PASJ: Publ. Astron. Soc. Japan **59**, S315–S325, 2007 January 25

Suzaku Observations of the Hard X-Ray Variability of MCG −6–30–15: the Effects of Strong Gravity around a Kerr Black Hole

Giovanni MINIUTTI,[1] Andrew C. FABIAN,[1] Naohisa ANABUKI,[2] Jamie CRUMMY,[1] Yasushi FUKAZAWA,[3] Luigi GALLO,[4,5] Yoshito HABA,[6] Kiyoshi HAYASHIDA,[2] Steve HOLT,[7] Hideyo KUNIEDA,[8] Josefin LARSSON,[1] Alex MARKOWITZ,[9] Chiho MATSUMOTO,[8] Masanori OHNO,[3] James N. REEVES,[9,10] Tadayuki TAKAHASHI,[5] Yasuo TANAKA,[4] Yuichi TERASHIMA,[5,11] Ken'ichi TORII,[2] Yoshihiro UEDA,[12] Masayoshi USHIO,[5] Shin WATANABE,[5] Makoto YAMAUCHI,[13] and Tahir YAQOOB[9,10]

[1]*Institute of Astronomy, University of Cambridge, Madingley Road, CB3 0HA Cambridge, UK*
miniutti@ast.cam.ac.uk
[2]*Department of Earth and Space Science, Osaka University, 1-1 Machikaneyama, Toyonaka, Osaka 560-0043*
[3]*Department of Physical Science, School of Science, Hiroshima University, 1-3-1 Kagamiyama, Higashi-Hiroshima, Hiroshima 739-8526*
[4]*Max-Planck-Institut für extraterrestrische Physik, Postfach 1312, Garching, Germany*
[5]*Institute of Space and Astronautical Science, Japan Aerospace Exploration Agency, Yoshinodai 3-1-1, Sagamihara, Kanagawa 229-8510*
[6]*Department of Astrophysics, Nagoya University, Furo-cho, Chikusa-ku, Nagoya 464-8602*
[7]*F. W. Olin College of Engineering, 1735 Great Plain Avenue, Needham, MA 02492, USA*
[8]*Department of Physics, Nagoya University, Furo-cho, Chikusa, Nagoya 464-8602*
[9]*Astrophysics Science Division, Code 662, NASA Goddard Space Flight Center, Greenbelt, MD 20771, USA*
[10]*Department of Physics and Astronomy, John Hopkins University, 3400 N Charles Street, Baltimore, MD 21218, USA*
[11]*Department of Physics, Ehime University, 2-5 Bunkyocho, Matsuyama, Ehime 790-8577*
[12]*Department of Astronomy, Kyoto University, Sakyo-ku, Kyoto 606-8502*
[13]*Department of Applied Physics, University of Miyazaki, 1-1 Gakuen-Kibanadi-Nishi, Miyazaki, Miyazaki 889-2192*

(Received 2006 August 18; accepted 2006 September 8)

Abstract

Suzaku has, for the first time, enabled the hard X-ray variability of the Seyfert 1 galaxy MCG −6–30–15 to be measured. The variability in the 14–45 keV band, which is dominated by a strong reflection hump, is quenched relative to that at a few keV. This directly demonstrates that the whole reflection spectrum is much less variable than the power-law continuum. The broadband spectral variability can be decomposed into two components — a highly variable power-law and constant reflection — as previously inferred from other observations in the 2–10 keV band. The strong reflection and high iron abundance give rise to a strong broad iron line, which requires the inner disc radius to be at about 2 gravitational radii. Our results are consistent with the predictions of the light bending model which invokes the very strong gravitational effects expected very close to a rapidly spinning black hole.

Key words: galaxies: active — galaxies: individual (MCG −6–30–15) — galaxies: Seyfert — X-rays: galaxies

1. Introduction

The Seyfert 1 galaxy MCG −6–30–15 at $z = 0.00775$ has been the centre of much interest since a broad iron line was discovered in its X-ray spectrum with the ASCA satellite (Tanaka et al. 1995). Iron line emission is part of the reflection spectrum produced by the hard X-ray power-law continuum in the source irradiating the accretion disc (Guilbert, Rees 1988; Lightman, White 1988; Ross, Fabian 1993) and is broadened and skewed by Doppler and gravitational redshift effects (Fabian et al. 1989). The low energy extent of the line can reveal the inner radius of the accretion disc and thus the black hole spin (for reviews see Fabian et al. 2000; Reynolds, Nowak 2003; Fabian, Miniutti 2006). The iron abundance in MCG −6–30–15 appears to be about 2 times the solar value (Fabian et al. 2002), making the iron line particularly strong.

MCG −6–30–15 was observed several more times with ASCA (Iwasawa et al. 1996, 1999; Matsumoto et al. 2003; Shih et al. 2002), by BeppoSAX (Guainazzi et al. 1999), RXTE (Lee et al. 1999; Vaughan, Edelson 2001), and by XMM-Newton (Wilms et al. 2001; Fabian et al. 2002; Fabian, Vaughan 2003; Vaughan, Fabian 2004). All of these observations confirmed the presence and general broad shape of the iron line. Evidence that the black hole in MCG −6–30–15 is rapidly spinning has been obtained from the extreme breadth of the line by Iwasawa et al. (1996), Dabrowski et al. (1997), Wilms et al. (2001), Fabian et al. (2002) and most recently Reynolds et al. (2005), who determine a spin parameter $a = 0.989$.

The XMM-Newton work emphasizes that much of the emission arise from smaller radii, between $2–6\,r_{\rm g}$ (where $r_{\rm g} = GM/c^2$). This may help to explain the otherwise puzzling spectral variations shown by the source. Shih et al. (2002), Fabian et al. (2002), Fabian and Vaughan (2003), and Taylor, Uttley, and McHardy (2003) found that the spectral variability can be explained by a simple two component model consisting of a highly variable power-law continuum (of almost fixed spectral slope) and a much less variable reflection spectrum, which of course includes the iron line. The reflection (and iron line) strength does not follow the power-law continuum intensity, as expected in a simple reflection picture. The

small radius of much of the emission can however explain this behaviour when it is recalled that as well as strong gravitational red-shifting occurring in this region, there is also strong gravitational light bending. This can disconnect variations in the continuum from those of the reflection and has led to the development of the light-bending model (Fabian, Vaughan 2003; Miniutti et al. 2003, 2004), which is a generalization of earlier work on the strong field regime (Martocchia, Matt 1996; Reynolds, Begelman 1997).

If the source of the continuum emission (assumed to be an isotropic emitter) changes location close to the black hole, then, even if the continuum has a constant intrinsic luminosity, it appears to the outside observer to change in brightness. This is just due to gravity bending the light rays out of the line of sight by different amounts depending upon the precise location of the source. Much of the radiation is bent down onto the disc, so the observed reflection intensity changes little. The two-component variability pattern and its light bending interpretation have recently found application in many other accreting black hole sources (Fabian et al. 2004, 2005; Miniutti et al. 2004; Ponti et al. 2006).

One striking feature of the model reflection spectrum is a large reflection hump peaking at 20–40 keV. This is where the disc albedo is highest; at lower energies the albedo is reduced by photoelectric absorption and at higher energies it is reduced (at a given energy) by Compton down-scattering of the photons (see e.g. George, Fabian 1991). The presence of the Compton hump has been confirmed in the spectrum of MCG −6–30–15 by BeppoSAX and RXTE observations (Guainazzi et al. 1999; Lee et al. 2000; Fabian et al. 2002). What those observations have not done is to determine the variability of the Compton hump and show that it varies in the same way as the rest of the reflection spectrum.[1] Here we carry out this important step with the Hard X-ray Detector (HXD) on Suzaku.

We concentrate on the Suzaku data above 3 keV since there is a complex warm absorber in MCG −6–30–15 (Otani et al. 1996; Lee et al. 2001; Turner et al. 2003, 2004). The difference spectrum between low and high states of the source shows that absorption is minimal above 3 keV (Fabian et al. 2002; Turner et al. 2004) and High Energy Transmission Grating (HETG) spectra from Chandra show no absorption feature around 6.5 keV which would indicate absorption by species of intermediate ionization which could affect our fits (Young et al. 2005).

2. The Suzaku Observations

MCG −6–30–15 was observed four times by Suzaku (Mitsuda et al. 2007), once between August 17–19 in 2005 for about 45 ks and three times in 2006 January with longer exposures. Here we focus on the three 2006 observations performed between 9–14 (150 ks), 23–26 (99 ks), and 27–30 (97 ks), in 2006 January. We use event files from revision 0.7 of the Suzaku pipeline. Version 0.7 processing is an internal processing applied to the Suzaku data obtained during the Suzaku Working Group phase, for the purpose of establishing the detector calibration as quickly as possible. Some processes that are not critical for most of the initial calibration and scientific studies, e.g., aspect correction, fine tuning of the event time tagging of the XIS data, are skipped in version 0 processing, making the quality of the products limited in these directions compared with the official data supplied to guest observers. The XIS data were screened with XSELECT as standard (see e.g. Koyama et al. 2007). The XIS products were extracted from circular regions of 4′.3 radius centred on the source, while background products were extracted from two smaller circular regions offset from the source (and avoiding the chip corners with calibration sources) with a total area equal to that of the source region. The latest response and ancillary response files provided by the instrument teams were used. For the HXD/PIN (Takahashi et al. 2007), instrumental background spectra were extracted from time dependent models provided by the HXD instrument team, based upon a database of non-X-ray background observations made by the PIN diode to date. Since the background modeling is the key issue for the hard X-ray measurement with the HXD, the HXD team has provided two independent background models, models A and B, which use different algorithms (Kokubun et al. 2007). Spectral analysis of the source spectrum using the two models was found to give statistically indistinguishable results for the three 2006 January MCG −6–30–15 observations over the whole 14–45 keV band used here, and we use the background model A in our analysis. The response files appropriate for the XIS nominal position observation were chosen dated as of 2006/08/07.

We have extracted products for the three front-illuminated CCD XIS detectors (XIS 0, XIS 2, and XIS 3) and for the back-illuminated CCD (XIS 1). The XIS 2 and XIS 3 detectors are found to produce remarkably similar spectra in the whole band used here. The XIS 0 spectrum is slightly flatter than that from the XIS 2 and XIS 3 detectors so we proceed by co-adding just the XIS 2 and XIS 3 products in our analysis [see Yaqoob et al. (2007) for mention of structures in the XIS 0 and XIS 1 spectra]. In figure 1, we show the broad-band 0.5–12 keV background subtracted light curve from the XIS 2 and XIS 3 detectors during the three pointed observations in 2006. We also show, as a reference, the count rate levels selected to define the High Flux (HF) and Low Flux (LF) states which will be used to study the spectral variability of MCG −6–30–15. As normal for this source [thought to harbour a black hole with a mass of $\sim 3 \times 10^6\, M_\odot$, McHardy et al. (2005)] the light curve exhibits large amplitude and relatively short timescale variability with variations up to factors 2–3 in a few kiloseconds.

3. The 3–12 keV XIS Spectrum

We start our analysis of the Suzaku data by considering the 3–12 keV time-averaged co-added spectrum from the XIS 2 and XIS 3 front-illuminated CCD detectors. (XIS response and ancillary files 20060213.rmf and 20060415.arf, with a 6 mm extract radius, were used.) The most important feature in this energy band is the strong, skewed, relativistic Fe Kα line which

[1] The possible anticorrelation between the reflection continuum and iron line reported by Lee et al. (2000) may in part be due to confusion caused by variation in the fitted power-law index [see discussion of a spurious reflection–photon index correlation found with RXTE data by Vaughan and Edelson (2001)].

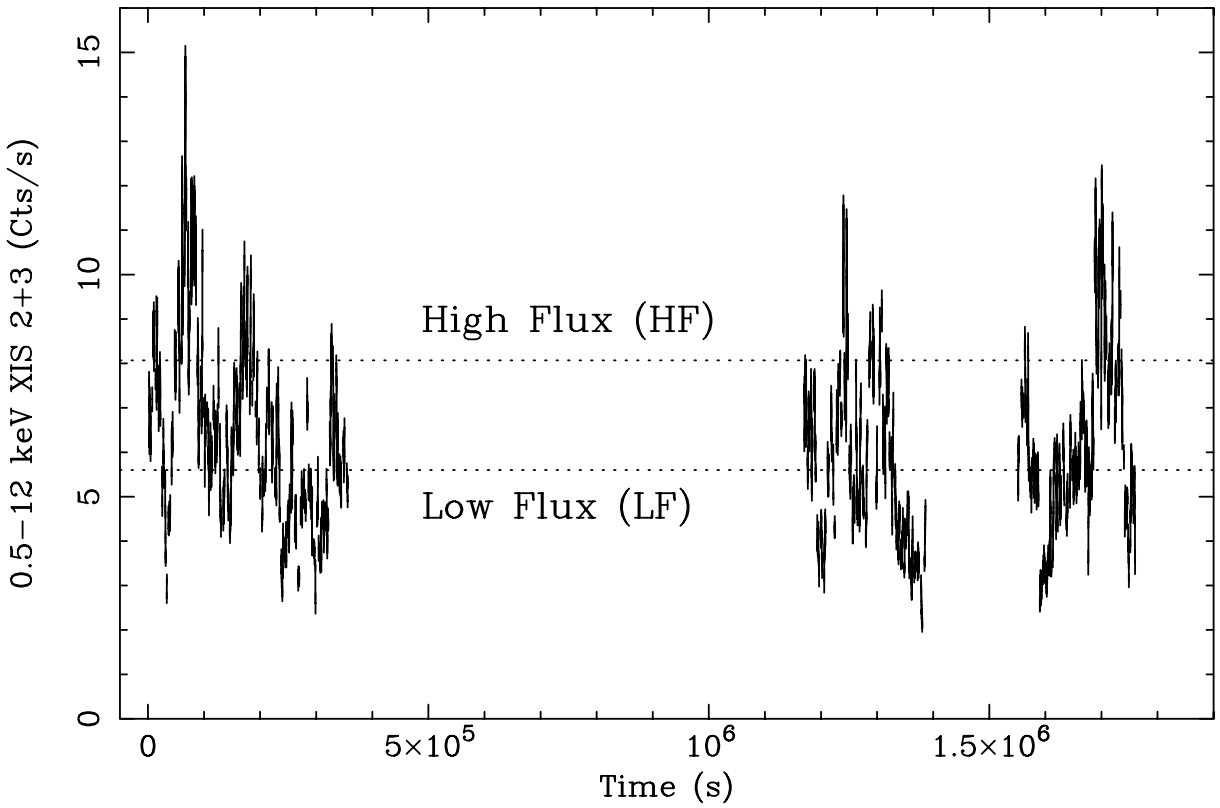

Fig. 1. The light curve from the XIS 2/XIS 3 detectors in the 0.5–12 keV band. We also show the count rates chosen to select the High Flux (HF) and Low Flux (LF) states. They are chosen so that the HF and LF spectra have approximately the same number of counts (6.5×10^5 in the whole 0.5–12 keV band).

characterizes the X-ray spectrum of MCG −6–30–15 enabling us to explore the nature and geometry of the accretion flow close to the central black hole with much higher accuracy than in any other object so far. In figure 2 we show the ratio of the data to a simple power law model fitted in the 3–4 keV and 7.5–12 keV bands and absorbed by the Galactic column density ($4.08 \times 10^{20}\,\mathrm{cm}^{-2}$). The residuals clearly show the asymmetric and broad Fe Kα line profile (top panel). In the bottom panel, we superimpose the Fe Kα profile as observed with the XMM-Newton EPIC–pn camera in 2001. The agreement between the two instruments is remarkable and demonstrates the excellent level of the Suzaku XIS calibration even in the early stages of the mission. The 2–10 keV flux is $4.1 \times 10^{-11}\,\mathrm{erg\,cm^{-2}\,s^{-1}}$ in the XMM-Newton observation and $4.0 \times 10^{-11}\,\mathrm{erg\,cm^{-2}\,s^{-1}}$ in the Suzaku one. Notice the absorption/emission structures in the blue wing of the relativistic line which are clearly detected by both the EPIC–pn and the XIS detectors with excellent agreement.

3.1. The Fe K Band and the Relativistic Line

As a first attempt to fit the Fe Kα line profile we consider the simplest possible spectral model comprising a power law continuum absorbed by a column of neutral matter (fixed at the Galactic value $N_{\mathrm{H}} = 4.08 \times 10^{20}\,\mathrm{cm}^{-2}$) and a set of Gaussian emission lines. We consider first three Gaussian emission lines: a narrow unresolved ~ 6.4 keV emission line (the narrow component of the Fe line from distant matter), two narrow unresolved ~ 6.7 keV and ~ 6.97 keV absorption lines (the Fe XXV and Fe XXVI resonant absorption line already detected by Chandra, Young et al. 2005), and an additional Gaussian emission line with width free to vary (representing the broad relativistic Fe line). We obtain a fit with $\chi^2 = 2550$ for 2235 degrees of freedom (dof). The narrow component of the Fe line is at $6.43^{+0.01}_{-0.02}$ keV (uncertainties are quoted throughout the paper at the 90% confidence level) and has an equivalent width (EW) of only 30 ± 5 eV. Absorption lines are detected at 6.74 ± 0.03 keV and 7.04 ± 0.05 keV. The broad Fe line is at 5.88 ± 0.05 keV, has a width of 840 ± 40 eV and an EW of 305 ± 20 eV.

However, the best-fitting model leaves clear residuals in the 3–12 keV band. In particular the broad Fe line is not properly modelled and the residuals suggest the introduction of a double Gaussian model with one broad Gaussian line around 6.4 keV and an even broader one at lower energies to model the extended red wing. We obtain a significant improvement of the statistics with $\chi^2 = 2398$ for 2232 (table 1). The energies of the three unresolved lines are $6.41^{+0.03}_{-0.02}$ keV for the narrow Fe emission line, and 7.04 ± 0.05 keV, and 6.73 ± 0.04 keV for the absorption lines. Their equivalent widths are 25 ± 5 eV, $-(12 \pm 8)$ eV, and $-(15 \pm 6)$ eV respectively. The upper limit on the EW of the narrow Fe Kα emission line (only 30 eV) indicates that reflection from distant matter plays a minor and marginal role in MCG −6–30–16, as already demonstrated by high-resolution spectroscopy with the HETG Chandra gratings (Lee et al. 2002; Young et al. 2005). The two absorption line energies are slightly higher than the

Table 1. Results of spectral fits to the 3–12 keV XIS 2 and XIS 3 time-averaged co-added spectrum with the different models used to describe the relativistic Fe line of MCG −6–30–15.*

Double Gaussian							
Continuum		Kα red wing			Kα blue core		χ^2/dof
Γ	E	σ	EW	E	σ	EW	
1.96 ± 0.02	5.38 ± 0.10	840^{+70}_{-80}	130 ± 15	$6.45^{+0.02}_{-0.05}$	290 ± 30	190 ± 30	2398/2232
Blurred Reflection							
Continuum		Relativistic blurring			Reflector		χ^2/dof
Γ	i	$r_{\rm in}$	$q_{\rm in}$	$q_{\rm out}$	R	ξ	
$2.18^{+0.07}_{-0.06}$	38 ± 4	$1.6^{+0.6}_{-0.365{\rm p}}$	$4.6^{+0.6}_{-0.9}$	2.6 ± 0.3	2.8 ± 0.9	65 ± 45	2360/2230

* We present results for a phenomenological double-Gaussian fit and for a much more self-consistent relativistically blurred reflection model. For the reflection model, we measure an Fe abundance of $2.0^{+1.4}_{-0.6}$ times solar. We only report results for the relativistic Fe line here. A more detailed fit is presented in table 2, where high-energy data from the HXD/PIN detector are also included. A subscript $_{\rm p}$ indicates that the parameter reached its min/max allowed value.

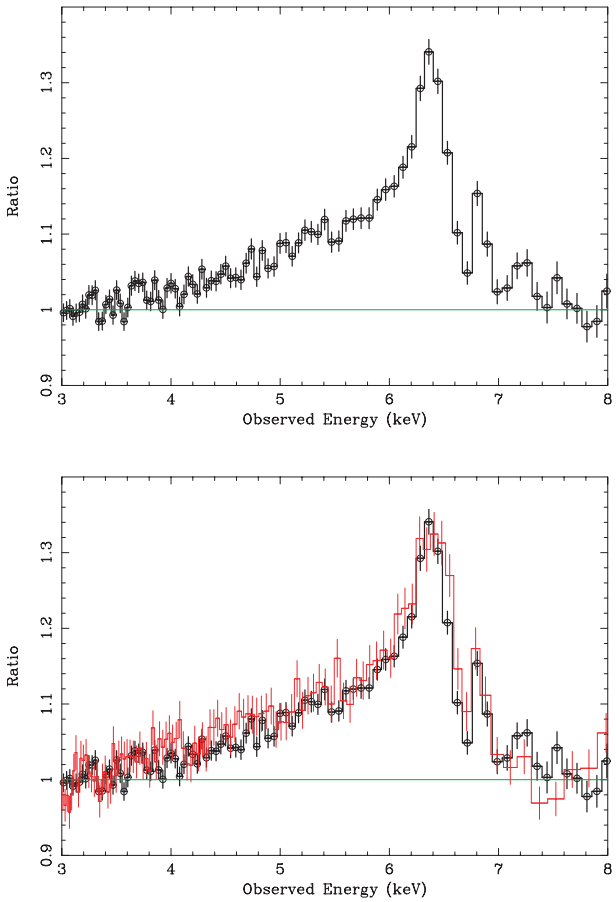

Fig. 2. Top: The Suzaku XIS data divided by a power law model fitted in the 3–4 keV and 7.5–10 keV bands are shown in the most relevant 3–8 keV band. Bottom: The data from the XMM-Newton EPIC–pn detector (half tone) are superimposed on the XIS data (black). In both cases the model is a power law absorbed by the Galactic column density and fitted in the 3–4 keV and 7.5–12 keV bands. Color figures are available in the on-line version.

rest-frame energies of Fe XXV and Fe XXVI resonant absorption and are consistent with an origin in a common outflow with velocity of few thousand km s^{-1}. In particular, they are both consistent in equivalent width and outflow velocity with the values measured with Chandra ($2.0^{+0.7}_{-0.9} \times 10^3$ km s^{-1}, Young et al. 2005). The photoelectric absorption implied by such a thin highly ionized absorber is small and has a negligible effect on the fits described here.

As for the broad Fe line, the parameters of the two broad Gaussian lines describing its profile are reported in table 1 (first model "Double Gaussian"). They are both clearly resolved and their cumulative EW is 320 ± 45 eV, although this value should be taken with care since the continuum is a simple absorbed power law and does not include the reflection continuum which must be associated with the broad Fe line. It is interesting to note that the width of the Fe line core at ~ 6.45 keV is $\sigma > 260$ eV (i.e. FWHM $\simeq 31950$ km s^{-1}) suggesting that it originates in the outer disc at $< 80\,r_{\rm g}$ from the central black hole, while the red wing has a width > 760 eV indicating that the emitting matter is located within $6.5\,r_{\rm g}$ from the centre, already implying, even by means of a very simple and phenomenological model, that the black hole in MCG −6–30–15 is most likely a spinning Kerr black hole in which the accretion disc extends down within the marginal stable orbit for a non-rotating Schwarzschild black hole ($6\,r_{\rm g}$).

3.2. *A Self-Consistent Reflection Model*

The multiple Gaussian fit described above is merely a phenomenological description of the hard spectrum. The Gaussian emission lines and, most importantly, the broad Fe line are the clear signature of X-ray reflection and the above spectral model did not include any reflection continuum. Here we build a much more self-consistent model in which the broad Fe line is computed together with the associated reflection continuum. We use a grid of models from Ross and Fabian (2005) to obtain the X-ray reflection spectrum. The X-ray reflection model has the spectral slope of the illuminating power law Γ, the ionization parameter ξ, the Fe abundance, and the normalization as free parameters. However, we forced the photon index to be the same as the power law continuum for consistency. Since the reflection model does not include Ni as an element, we also include a Ni Kα line with energy fixed at 7.47 keV.

In order to reproduce the relativistic broad Fe line profile, the reflection spectrum is convolved with a relativistic kernel derived from the Laor (1991) code. The relativistic blurring

parameters are the emissivity indexes $q_{\rm in}$ and $q_{\rm out}$ (where the emissivity is $\epsilon = r^{-q_{\rm in}}$ within the innermost $6\,r_{\rm g}$ and $\epsilon = r^{-q_{\rm out}}$ outside), the inner disc radius $r_{\rm in}$, and the observer inclination i. The outer disc radius is fixed at its maximum allowed value of $400\,r_{\rm g}$. The choice of a broken power law emissivity profile is motivated by the previous long XMM-Newton observation of MCG −6–30–15 (Vaughan, Fabian 2004).

The model is applied to the co-added XIS 2 and XIS 3 time-averaged spectrum in the 3–12 keV band and we keep the three unresolved Gaussian lines as above. The results of the spectral fitting are reported in table 1 ("Blurred Reflection" model). We obtain a better fit with $\chi^2 = 2360$ for 2230 dof. The better fit with respect to the phenomenological Double Gaussian model described above is due to a better description of the overall relativistic Fe line profile. In addition, the model accounts for some high-energy residuals above about 10 keV which were present in the above best-fitting solution due to the unmodelled reflection component.

We measure a relatively standard $\Gamma = 2.18^{+0.07}_{-0.06}$ continuum slope which compares very well with previous results with XMM-Newton. The reflection component contributes significantly to the hard spectrum of MCG −6–30–15 and we measure a reflection fraction of $R = 2.8 \pm 0.9$ ($R = 1$ corresponds to the level of reflection expected from 2π sr), fully consistent with previous results from a simultaneous XMM-Newton and BeppoSAX observation (Vaughan, Fabian 2004). The precise value of the reflection fraction will be better constrained in a subsequent analysis when the high energy data from the HXD/PIN detector are considered as well. The reflector is only mildly ionized with $\xi = 65 \pm 45\,{\rm erg\,cm\,s^{-1}}$ and the inclination is constrained to be $38^\circ \pm 4^\circ$.

As for the relevant relativistic blurring parameters, the XIS data are able to constrain the inner disc radius to be smaller than $r_{\rm in} < 2.2\,r_{\rm g}$. If, as it is customary, $r_{\rm in}$ is identified with the innermost stable circular orbit around a Kerr black hole, such a small 90% upper limit implies that the black hole spin in MCG −6–30–15 is $a > 0.917$, i.e., the black hole is an almost maximally spinning Kerr black hole. The inner and outer emissivity profiles are not consistent with each other within the errors and $q_{\rm in} \simeq 4.8$ is steeper than $q_{\rm out} \simeq 2.6$. However, if the two indices are forced to be one and the same, we obtain $q_{\rm in} \equiv q_{\rm out} = 3.1^{+0.5}_{-0.3}$ with only a slight worsening of the fit statistic ($\Delta\chi^2 = 6$).

4. Adding the HXD/PIN Data; the 3–45 keV Spectrum

In the above analysis the relativistic Fe line is associated with its own reflection continuum and a self-consistent model to the 3–12 keV spectrum is found. However, one of the main characteristics of the Suzaku mission is the presence of the HXD PIN hard X-ray detector providing high quality data above 12 keV (figure 3). The spectral analysis of the XIS data revealed the presence of a strong reflection component associated with the broad relativistic Fe line which would produce a strong Compton hump around 20–30 keV. The HXD data above 12 keV are thus crucial to investigate the reflection component further and will enable us to infer the reflection parameters and to measure the direct and reflection continua with high accuracy.

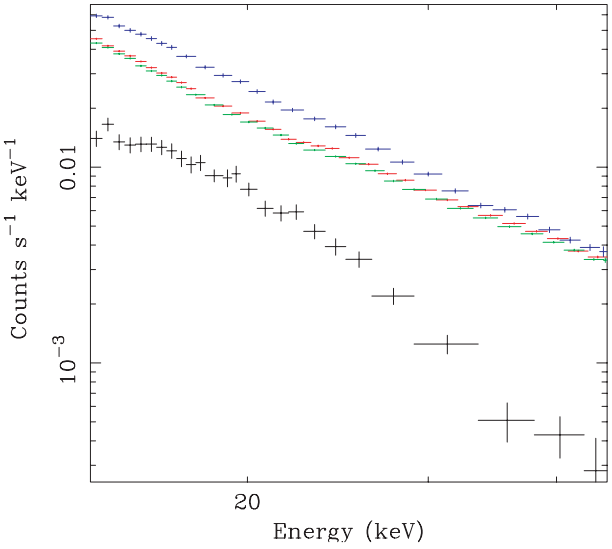

Fig. 3. PIN data displayed as total count rate (upper), backgrounds A and B (respectively, middle), and source (lower) spectra.

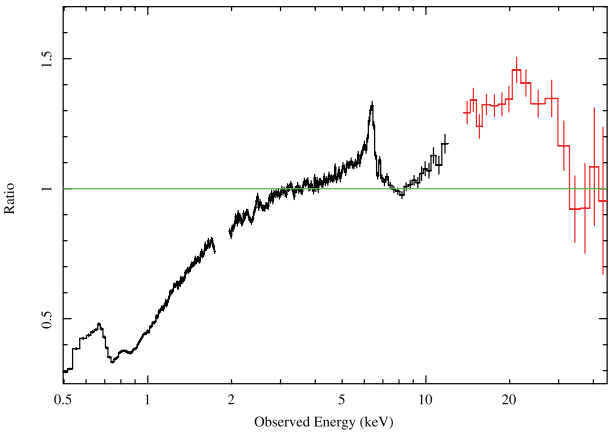

Fig. 4. The XIS 2/XIS 3 and PIN data in the 0.5–45 keV band are compared with a simple power law fitted in the 3–45 keV band ignoring the Fe K and Compton hump energy bands (4–7.5 keV and 14–30 keV). The ratio plot shows the main spectral components which are the power law continuum, absorption below about 3 keV, and a strong smeared reflection component comprising the relativistic broad Fe line and Compton hump. Data have been re-binned for visual clarity.

In figure 4, we show the XIS and HXD/PIN time-averaged spectrum in the 0.5–45 keV band. The figure shows the data to model ratio for a power law model fitted above 3 keV and ignoring the bands where reflection is expected to dominate. The ratio clearly shows the presence of both the relativistic Fe line in the XIS data and also the presence of a large Compton hump around 20 keV visually confirming that the hard spectrum of MCG −6–30–15 is dominated by a strong reflection component. Absorption is present affecting the soft band below 3 keV. We avoid the complication of modelling the complex warm absorber and we concentrate, in this first paper on the Suzaku observation of MCG −6–30–15, on the data above 3 keV. A detailed model of the warm absorber will be presented elsewhere where the data from the back-illuminated

Table 2. Results of fits to the XIS 2/XIS 3 and PIN Time-Averaged (TA), High Flux (HF), and Low Flux (LF) spectra in the 3–45 keV band.*

Parameter	TA spectrum	HF spectrum	LF spectrum
Γ	2.26 ± 0.04	2.25 ± 0.05	2.25 ± 0.05
$N_{\rm PL}$	1.7 ± 0.1	2.7 ± 0.1	1.2 ± 0.1
R	3.8 ± 0.7	2.5 ± 0.6	4.8 ± 0.8
ξ	68 ± 31	70 ± 37	48 ± 35
$A_{\rm Fe}$	$1.9^{+1.4}_{-0.5}$	$1.8^{+1.3}_{-0.4}$	$1.9^{+1.5}_{-0.6}$
$r_{\rm in}$	$1.7^{+0.4}_{-0.465{\rm p}}$	$1.235^{+0.7}_{-0.0{\rm p}}$	$1.7^{+0.3}_{-0.465{\rm p}}$
i	38 ± 3	37 ± 4	41 ± 5
$q_{\rm in}$	$4.4^{+0.5}_{-0.8}$	$3.6^{+0.8}_{-0.7}$	4.5 ± 0.6
$q_{\rm out}$	2.5 ± 0.3	2.8 ± 0.4	2.6 ± 0.3
$E_{\rm Fe\ K\alpha}$	$6.41^{+0.03}_{-0.02}$	6.40 ± 0.03	6.41 ± 0.03
${\rm EW}_{\rm Fe\ K\alpha}$	35 ± 5	19 ± 4	44 ± 6
$N_{\rm Fe\ K\alpha}$	8.5 ± 1.3	8.3 ± 1.2	8.5 ± 1.3
$E_{\rm abs_1}$	6.73 ± 0.04	6.72 ± 0.05	6.75 ± 0.04
${\rm EW}_{\rm abs_1}$	$-(22 \pm 8)$	$-(20^{+23}_{-14})$	$-(45 \pm 30)$
$E_{\rm abs_2}$	7.07 ± 0.04	7.08 ± 0.05	7.03 ± 0.04
${\rm EW}_{\rm abs_2}$	$-(13 \pm 8)$	$-(15 \pm 10)$	$-(28 \pm 18)$
$F^{\rm PL}_{\rm 3-45\,keV}$	4.0 ± 0.2	6.4 ± 0.2	2.9 ± 0.3
$F^{\rm REF}_{\rm 3-45\,keV}$	4.1 ± 0.8	4.0 ± 0.9	3.8 ± 0.6
χ^2/dof	2495/2312	1910/1848	1900/1925

* The power law normalization ($N_{\rm PL}$) is given in units of $10^{-2}\,{\rm ph\,cm^{-2}\,s^{-1}}$. As for the reflection, we prefer to give the reflection fraction which is a more interesting measure of its strength. The power law and reflection fluxes are reported in the 3–45 keV band in units of $10^{-11}\,{\rm erg\,cm^{-2}\,s^{-1}}$ for completeness. The reflector ionization parameter (ξ) is in ${\rm erg\,cm\,s^{-1}}$ and the inner disc radius ($r_{\rm in}$) and inclination (i) are in units of $r_{\rm g} = GM/c^2$ and degrees respectively. The energies of the lines are in keV, their EW in eV, and their width is fixed to 10 eV. The narrow Fe Kα normalization is in units of $10^{-6}\,{\rm ph\,cm^{-2}\,s^{-1}}$. A subscript $_{\rm p}$ indicates that the parameter reached its min/max allowed value.

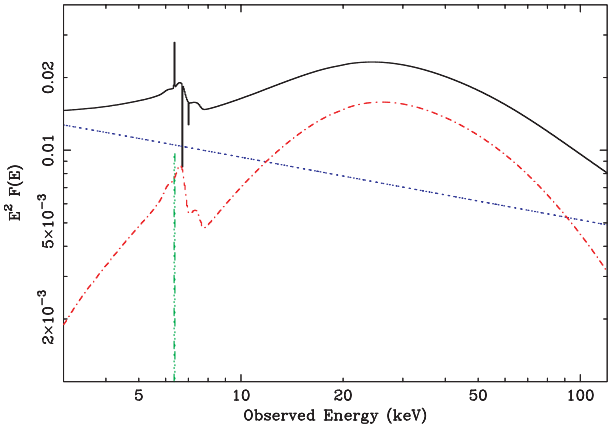

Fig. 5. The best-fit model components to the time-averaged spectrum of MCG −6–30–15.

(more sensitive at soft energies) XIS detector will be also considered.

We consider our best-fitting spectral model to the 3–12 keV XIS data and extend it to the PIN data between 14 keV and 45 keV. We include a cross-normalization constant between the XIS and PIN data and find that it is constrained to be 1.10 ± 0.05 (where the XIS constant is set to 1). This factor is consistent with the results obtained from Crab observations (Kokubun et al. 2006). Since the available HXD/PIN background model A does not include the contribution from the X-ray cosmic background, a spectral model of the form $2.06 \times 10^{-6}(E/100{\rm keV})^{-1.29}\exp(-E/41.13{\rm keV})$ was included in all spectral fits in the HXD/PIN band (the model being valid up to about 70 keV). The model is based on the HEAO-A1 spectrum, re-scaled to account for the HXD field of view.

The best-fitting XIS model provides an acceptable description of the 3–45 keV data and we obtain a good quality fit of $\chi^2 = 2495$ for 2312 dof. The model parameters are very much consistent with those obtained from the 3–12 keV parameters. In fact, extending the model up to 45 keV provides a reasonable description of the hard data, reproducing most of the large Compton hump seen in figure 4, even before fitting. The results for the Time-Averaged (TA) spectrum in the 3–45 keV band are reported in table 2 together with similar fits to the High Flux (HF) and Low Flux (LF) spectra which will be discussed below (figure 5). The reflection component contributes significantly to the total flux and we measure a large reflection fraction of 3.8 ± 0.7. As a reference, and since it will be useful in a spectral variability analysis below, we report here that its contribution represents the $33 \pm 6\%$ of the total flux in the 3–12 keV band and the $51 \pm 10\%$ in the 14–45 keV band. The relativistic blurring parameters are consistent within the errors with those already reported in table 1 and the same is true for the continuum power law slope and for the ionization parameter.

As a consistency check, we have also determined the level of the reflection component by using the spectrum above 7.5 keV, so avoiding the iron line. For this the `pexrav` model in XSPEC was used, with results $\Gamma = 2.2$, reflection fraction $R = 2$–4 and iron abundance poorly constrained ($A_{\rm Fe} = 0.5$–2 times solar). We note that such reflection predicts a *strong* iron line with an equivalent width of at least 300 eV (taking conservatively an iron abundance of unity and reflection fraction of 2), using the predictions of George and Fabian (1991). The limit on any narrow component to the iron emission feature is at least ten times smaller than this (this work; Lee et al. 2002; Young et al. 2005), thereby ruling out any non-smeared origin for the reflection component. The reflection must be due to matter well within the optical broad line region. We also stress that if the evidence for relativistic reflection is taken into account and the `pexrav` component is blurred accordingly, the shape of the reflection continuum is broader and redshifted requiring a higher Fe abundance ($A_{\rm Fe} = 1.5$–3.5 times solar) and reflection fraction ($R = 3$–5) to fit the data, while the continuum photon index is basically unaffected. The blurred and Fe overabundant reflector described by `pexrav` is thus fully consistent with our best-fitting results with a much more complex spectral model including the relativistic Fe line (see table 2).

5. Flux and Spectral Variability

The HXD/PIN detector has no imaging capabilities and thus there is no simple way to obtain a background subtracted light curve by selecting appropriate regions. However, background subtracted light curves can be obtained by extracting spectra in each time interval, subtracting the background from the available models in the same time interval, and reading out the background subtracted count rate. In background model A, the background of the HXD is calculated from the data base by using the count rate of the upper discriminator, which has a strong correlation with the flux of the non-X-ray background. The procedure must also include a model for the cosmic X-ray background (not included in the available background models) and we use the same model as for spectral fitting by simulating the cosmic X-ray background HXD/PIN spectrum and adding it to the instrumental background. We have applied the above procedure to the HXD/PIN data by selecting, after some experimentation, a timescale of 45 ks enabling us to obtain about 5000 background subtracted counts per time interval in the 14–45 keV PIN band on average. In figure 6 we show the XIS 2 and XIS 3 and the HXD/PIN light curves for the three 2006 observations in the 0.5–12 keV and 14–45 keV respectively. To ease the comparison, the XIS light curves have been re-scaled so that they have the same mean count rate as the PIN ones in each segment (i.e. observation). It is visually clear that the harder band (solid red) has a much lower variability amplitude than the softer one (dotted black). In the following we explore a set of different techniques with the aim of exploring the flux and spectral variability of the source.

5.1. *Flux–Flux Plots*

As a first model-independent way to characterize the flux/spectral variability of MCG −6–30–15 we analysed the relationship of the fluxes (count rates) in different energy bands following the technique of flux–flux plots introduced by Churazov, Gilfanov, and Revnivtsev (2001) in a study of Cygnus X-1 spectral variability, and Taylor, Uttley, and McHardy (2003) as a model-independent tool to disentangle the main drivers of the spectral variability in AGN.

In figure 7 we show the 3–12 keV XIS count rate from the 45 ks light curve against the count rate in the 1–2 keV band which is chosen as reference (see also Vaughan, Fabian 2004). The relationship between the count rates in the two bands is remarkably linear and leaves a clear hard offset on the y-axis, as already noticed by Taylor, Uttley, and McHardy (2003) and Vaughan and Fabian (2004) in previous RXTE and XMM-Newton observations. The linearity of the relationship indicates that the flux variations are strongly dominated by changes in the normalization of a spectral component with constant spectral shape. On the other hand, the hard offset suggests the presence of a component that varies little and that contributes more to the hard than to the reference 1–2 keV band. We measure a hard offset of $a = 0.48 \pm 0.02\,\mathrm{cts\,s^{-1}}$ which can be used to infer the contribution of the weakly variable component at mean flux level: since the mean count rate in the 3–12 keV band is $1.79 \pm 0.01\,\mathrm{cts\,s^{-1}}$, the hard offset a represents $26.8^{+1.3}_{-1.2}\%$ of the 3–12 keV flux at mean flux level. This compares very well with the $33 \pm 6\%$ contribution of the reflection component to the 3–12 keV band, as obtained from direct spectral fitting.

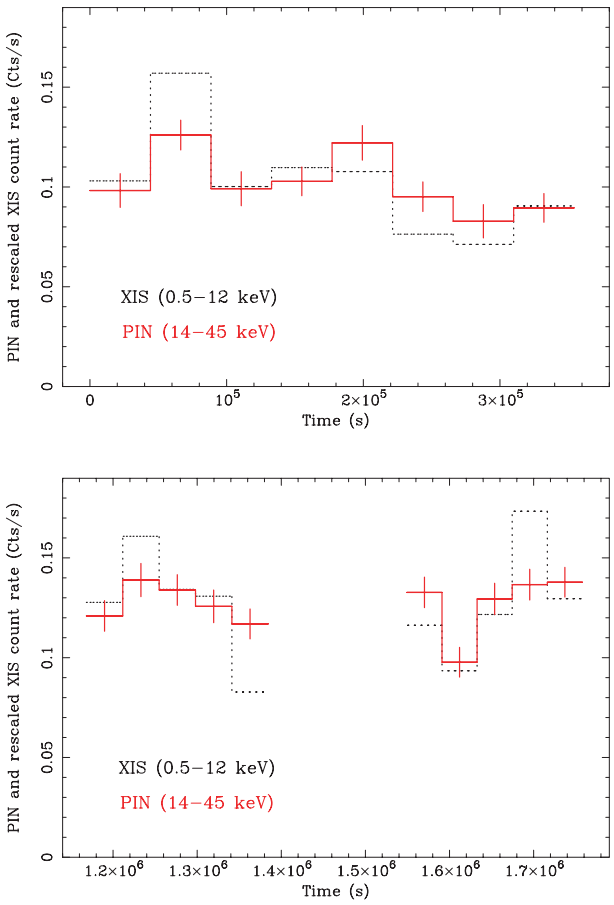

Fig. 6. The background subtracted light curve of MCG −6–30–15 during the three 2006 pointed observations (first in the top panel, second and third in the bottom panel). The dotted black light curve is the XIS 2 and XIS 3 light curve rescaled to the mean HXD/PIN count rate in each orbit. In halftone (red), we show the HXD/PIN light curve. The time bin is about 45 ks. Time elapses from the start of the first observation.

We have applied the same technique to the HXD/PIN light curve and plotted the 14–45 keV count rate against the 1–2 keV reference one. The relationship is much more noisy than when data from the XIS alone were used. To reduce the scatter and decrease the PIN error bars, we have binned the original flux–flux plot according to the soft reference count rate so that each new point comprises three original data points. In the lower panel of figure 7 we show the binned flux–flux plot obtained by plotting the 14–45 keV HXD/PIN count rate against the reference 1–2 keV one.

A fit with a linear relationship is perfectly acceptable ($\chi^2 = 5.8$ for 5 dof), again indicating the presence of a clear hard offset in the PIN band. In this case, the contribution of the weakly variable (reflection) component to the 14–45 keV band at mean flux level is estimated to be as high as $55 \pm 17\%$. Again, this is in good agreement with the contribution of the reflection component in the 14–45 keV band obtained from direct spectral fitting ($51 \pm 10\%$).

The flux–flux plot analysis detailed above indicates that the

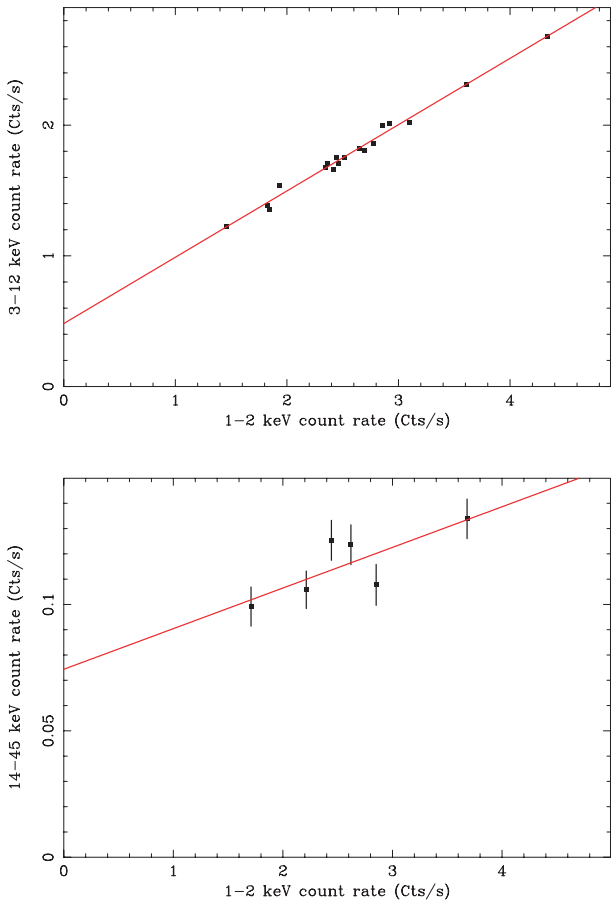

Fig. 7. Top: The XIS 2 and XIS 3 count rate in the hard 3–12 keV band is plotted against that in the 1–2 keV band from the 45 ks light curve. The relationship is linear and reveals a clear hard off-set. Bottom: Flux–flux plot for the 14–45 keV HXD/PIN data against the 1–2 keV reference band. Due to larger spread in the PIN band (see text for details), we have re-binned the original flux–flux plot according to the 1–2 keV flux so that each data point shown here comprises three original data points. The binned flux–flux plot exhibits a linear relationship, although some scatter is present.

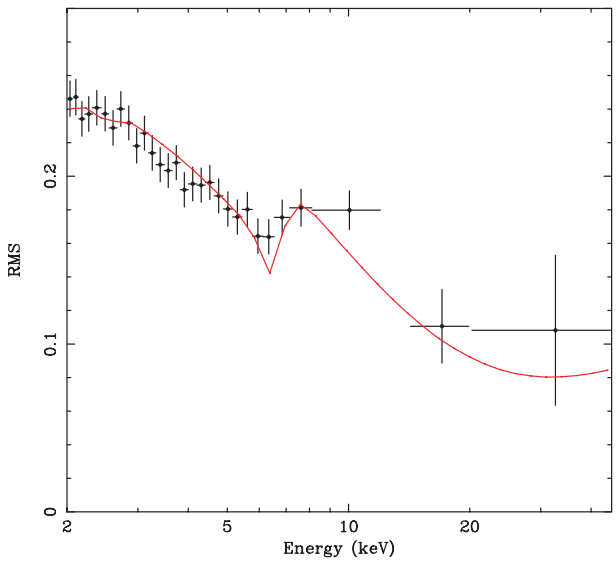

Fig. 8. The RMS spectrum of MCG −6–30–15 on a 45 ks timescale is shown in the 2–45 keV band. The solid line represents the theoretical RMS that would be obtained from the best-fitting spectral model of the time-averaged spectrum if all the variability could be explained with a two-component model in which the power law has a constant photon index and varies in normalization only, while the disc reflection component is perfectly constant.

spectral variability of MCG −6–30–15 can be decomposed into two main components: a highly variable component which varies in normalization only but not in spectral shape, and a weakly variable one which has a much harder spectral shape. The excellent agreement between the contribution of the weakly variable component in the different energy bands as inferred from the flux–flux plot analysis and that of the reflection component as obtained by direct spectral fitting strongly suggest that the weakly variable component is the relativistically smeared X-ray reflection from the accretion disc. Obviously, the highly variable component can be identified with the other component required by spectral fitting, i.e. the power law continuum. The flux–flux plots suggest that as the source varies, the power law maintains the same spectral slope and only varies in normalization.

5.2. *The Flux RMS Spectrum*

A further approach to studying the spectral variability of a source is the RMS spectrum, which, for a chosen timescale, is the fractional variability seen at each energy expressed as a flux normalized root mean square variability function. The RMS spectrum allows us to quantify the fractional variability as a function of energy in a model-independent manner and is therefore an important piece of information, complementary to the flux–flux plot analysis described above. Such RMS spectra have previously been determined for MCG −6–30–15 (Matsumoto et al. 2003; Fabian et al. 2002; Ponti et al. 2004). However, as far as data below 10 keV are available, the RMS spectrum has proved to be ambiguous to model. In particular, the typical trend that is observed in AGN is that the fractional variability decreases with energy, a behaviour that can be explained either in terms of a power law softening at high flux levels (i.e., a pivoting power law) or in the framework of the two-component model discussed above. The new ingredient here is to include the HXD/PIN data above 10 keV with the goal of confirming/rejecting the interpretation that comes out from the flux–flux plots analysis.

Our result for a 45 ks timescale is shown in figure 8. The general trend is that the RMS decreases with energy with a marked drop at ~ 6.4 keV reassuringly confirming that the Fe line is less variable than the continuum, as already noticed in previous works (e.g. Vaughan, Fabian 2004; Ponti et al. 2004). The novelty of the Suzaku observation is represented by the HXD/PIN data. They confirm the trend of lower fractional variability at higher energies but they lie above and not on the extrapolation of the 2–6 keV trend.

We have theoretically modelled the RMS spectrum by considering our best-fitting spectral model to the time-averaged spectrum and reproducing the 45 ks data by allowing only the power law normalization to vary, i.e. enforcing a perfect two-component model. The result of this exercise is shown as a

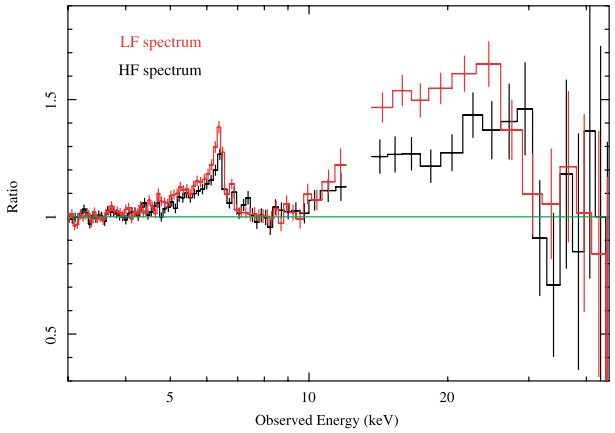

Fig. 9. Ratio plot for the HF (black) and LF (halftone) spectra with a power law model fitted ignoring the 4–7.5 keV and 14–30 keV energy bands. The ratio shows that the Compton hump contributes by about 60% in the LF state and by about 30% in the HF one, while its contribution in the time-averaged spectrum is about 40% (see figure 4). This shows that the reflection component is less variable than the power law and thus, the reflection fraction increases as the overall flux decreases.

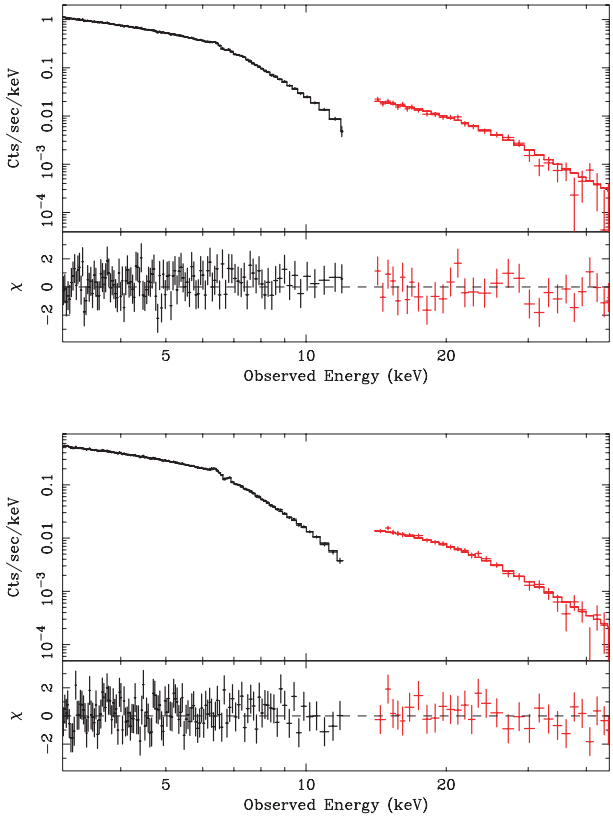

Fig. 10. The spectra, best-fitting model, and residuals for the HF (upper panel) and LF (lower panel) states.

solid line in figure 8 and shows that the RMS spectrum is fully consistent with a two-component model in which the only variable component is a constant-slope power law. Some variability of the reflection component cannot be excluded, but its variability amplitude is certainly not comparable to the variability amplitude of the power law. Indeed, small mismatches between the model and the data could be due to some intrinsic variability of the reflection component which deserves more detailed study to be performed in future work.

5.3. *The High and Low Flux States*

Having analysed the spectral variability of MCG −6–30–15 with two model-independent (and calibration-independent) techniques we now consider a more direct approach through spectral fitting. We extracted High Flux (HF) and Low Flux (LF) from both the XIS and the PIN spectra according to the selection criterion shown in figure 1. We first consider a simple power law fit in the 3–45 keV band ignoring, as done before, the Fe K and Compton hump bands. The result for the HF and LF spectra is shown in figure 9 as a ratio plot. There is a clear evidence, both in the XIS and in the HXD/PIN, that the reflection component contributes more to the LF than to the HF spectrum, which again indicates an almost constant reflection.

We have then applied the same spectral model as for the 3–45 keV time-averaged (TA) spectrum to the HF and LF spectra and our results are reported in table 2. Almost all parameters are consistent with being the same in the HF and LF spectra. In particular, the power law slope is consistent with being constant and equal to ~ 2.25 in the TA, HF, and LF spectra. The same is true for the Fe abundance, disc inclination, inner disc radius, outermost emissivity index $q_{\rm out}$, and reflector ionization state (although there is some indication for a lower ionization at low flux levels). The innermost emissivity index $q_{\rm in}$ appears to be steeper in the LF than in the HF spectrum, but the two indexes are still consistent with each other within the 90% errors. A steeper emissivity profile in the LF state would produce a more extended red wing as expected in the framework of the light bending model where low flux states are characterized by a more centrally concentrated illumination of the inner disc.

On the other hand, the reflection fraction definitely appears to vary and it is higher in the LF spectrum ($R = 4.8 \pm 0.8$) than in the HF one ($R = 2.5 \pm 0.6$) as already strongly suggested by the ratio plot in figure 9. This result is fully consistent with the indication inferred from the flux–flux plot and rms spectrum analysis discussed above: if the reflection component is only weakly variable, its contribution increases in the LF states because the direct power law decreases while the reflection stays approximately constant. We point out that this is exactly the behaviour predicted by the light bending model (Miniutti, Fabian 2004). The spectra, best-fitting models and residuals for the HF and LF states are shown in figure 10. The best-fit spectral components are as in figure 5 (which refers to the best-fit parameters to the time-averaged spectrum) with the only major difference in the HF/LF state being due to a higher/lower power law normalization.

5.4. *The Difference Spectrum*

We also produced a difference spectrum obtained by subtracting the LF spectrum from the HF one for the XIS and HXD/PIN. By definition, the difference spectrum only shows the variable components of the spectrum (modified by absorption), while any non-variable component is subtracted away. In figure 11 we show the residuals to a simple power law fit in

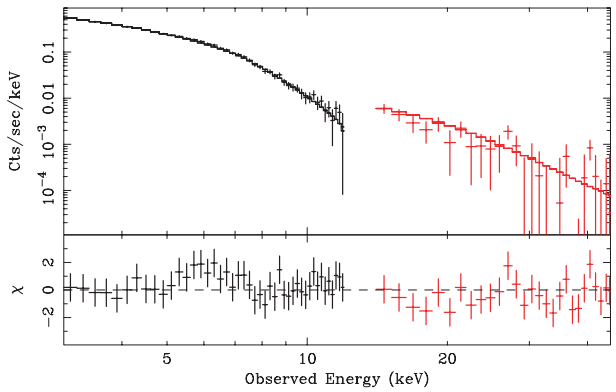

Fig. 11. The difference spectrum (HF minus LF) fitted with a power law absorbed by the Galactic column.

the 3–45 keV band where Galactic absorption is included. The power law fit is very good and the power law slope is consistent with that found in our spectral analysis ($\Gamma = 2.2 \pm 0.1$) but clear positive residuals are left in a broad hump around 6 keV at the $\sim 2\sigma$ level. This may indicate either that the red wing of the relativistic Fe line has varied in flux or that the shape of the line is slightly different in the HF and LF spectra.

If the residuals are due to flux variability of the reflection component, we should also see some positive residuals at the Compton hump energy (20–30 keV) which are not seen in the HXD/PIN difference spectrum. Some reflection variability is in fact allowed by the results of our spectral fits of the HF and LF spectra (see table 2) although the reflection flux is consistent with being the same at the two flux levels. If the reflection flux varied but the Fe line keeps the same shape, the main residual in the difference spectrum should be at the energy of the blue peak of the line, around 6.4 keV, while the residuals in figure 11 indicate that only the red wing of the line has varied.

The remaining possibility is that the Fe line has a different shape (rather than a different flux) in the HF and LF spectra. This is already hinted at by the inner emissivity index ($q_{\rm in}$, see table 2) which is marginally steeper in the LF state (although consistent within the errors). If the emissivity is really different at the two flux levels, residuals are produced in the red wing of the line and could potentially explain those seen in the difference spectrum (and at the same time the lack of residual at Compton hump energies). The result is in the sense expected from the light-bending model (see figure 4 of Miniutti, Fabian 2004).

6. Discussion

The Suzaku observation of MCG −6–30–15 has, for the first time, enabled the hard X-ray variability of the source to be determined. A wide range of techniques including direct spectral fitting, flux-flux and rms plots all show that the spectral variability on a 45 ks timescale can be decomposed into just two broad components above 3 keV, namely a variable power-law continuum and a harder constant component. This last component has the broad iron line and reflection hump expected from X-ray reflection in the very innermost regions of an accretion disc around a rapidly spinning black hole.

Just the strength and shape of the reflection component predict a high equivalent width iron line, much stronger than the weak narrow emission component seen in the spectrum. The only way for such a strong iron line to be 'hidden' in the spectrum is for it to be smeared into the broad emission structure that we observe.

The behaviour of the power-law and reflection components is consistent with the light bending model. In which case much of the rapid (power-law component) variability seen in the source is due to strong gravitational light bending as the site of the emission region changes location within a few gravitational radii of the black hole. We assume that the emission region is associated with some magnetic structure produced by the strong differential motions in the accretion disc. Note that to produce observed variability the emission region does not need to physically move, just that the main emission site changes position.

The broad iron line is strong in MCG −6–30–15 because both the iron abundance is high, at around 2 times the solar value, and the large degree of light bending around its Kerr black hole has emphasised the reflection spectrum relative to the power-law continuum.

We are deeply grateful to the whole Suzaku team for building, launching, calibrating, and operating the spacecraft and instruments. GM thanks the UK PPARC for support. ACF thanks the Royal Society, JL thanks the Isaac Newton Trust, Corpus Christi College and the UK PPARC, JC thanks the UK PPARC for support.

References

Churazov, E., Gilfanov, M., & Revnivtsev, M. 2001, MNRAS, 321, 759
Dabrowski, Y., Fabian, A. C., Iwasawa, K., Lasenby, A. N., & Reynolds, C. S. 1997, MNRAS, 288, L11
Fabian, A. C., et al. 2002, MNRAS, 335, L1
Fabian, A. C., Iwasawa, K., Reynolds, C. S., & Young, A. J. 2000, PASP, 112, 1145
Fabian, A. C., & Miniutti, G. 2006, in Kerr Spacetime: Rotating Black Holes in General Relativity, ed. D. L. Wiltshire, M. Visser, & S. M. Scott (Cambridge UK: Cambridge Univ. Press) in press (astro-ph/0507409)
Fabian, A. C., Miniutti, G., Gallo, L., Boller, Th., Tanaka, Y., Vaughan, S., & Ross, R. R. 2004, MNRAS, 353, 1071
Fabian, A. C., Miniutti, G., Iwasawa, K., & Ross, R. R. 2005, MNRAS, 361, 795
Fabian, A. C., Rees, M. J., Stella, L., & White, N. E. 1989, MNRAS, 238, 729
Fabian, A. C., & Vaughan, S. 2003, MNRAS, 340, L28
George, I. M., & Fabian, A. C. 1991, MNRAS, 249, 352
Guainazzi, M., et al. 1999, A&A, 341, L27
Guilbert, P. W., & Rees, M. J. 1988, MNRAS, 233, 475
Iwasawa, K., et al. 1996, MNRAS, 282, 1038

Iwasawa, K., Fabian, A. C., Young, A. J., Inoue, H., & Matsumoto, C. 1999, MNRAS, 306, L19
Kokubun, M., et al. 2007, PASJ, 59, S53
Koyama, K., et al. 2007, PASJ, 59, S23
Laor, A. 1991, ApJ, 376, 90
Lee, J. C., et al. 2001, ApJ, 554, L13
Lee, J. C., Fabian, A. C., Brandt, W. N., Reynolds, C. S., & Iwasawa, K. 1999, MNRAS, 310, 973
Lee, J. C., Fabian, A. C., Reynolds, C. S., Brandt, W. N., & Iwasawa, K. 2000, MNRAS, 318, 857
Lee, J. C., Iwasawa, K., Houck, J. C., Fabian, A. C., Marshall, H. L., & Canizares, C. R. 2002, ApJ, 570, L47
Lightman, A. P., & White, T. R. 1988, ApJ, 335, 57
Martocchia, A., & Matt, G. 1996, MNRAS, 282, L53
Matsumoto, C., Inoue, H., Fabian, A. C., & Iwasawa, K. 2003, PASJ, 55, 615
McHardy, I. M., Gunn, K. F., Uttley, P., & Goad, M. R. 2005, MNRAS, 359, 1469
Miniutti, G., & Fabian, A. C. 2004, MNRAS, 349, 1435
Miniutti, G., Fabian, A. C., Goyder, R., & Lasenby, A. N. 2003, MNRAS, 344, L22
Miniutti, G., Fabian, A. C., & Miller, J. M. 2004, MNRAS, 351, 466
Mitsuda, K., et al. 2007, PASJ, 59, S1
Otani, C., et al. 1996, PASJ, 48, 211
Ponti, G., Cappi, M., Dadina, M., & Malaguti, G. 2004, A&A, 417, 451
Ponti, G., Miniutti, G., Cappi, M., Maraschi, L., Fabian, A. C., & Iwasawa, K. 2006, MNRAS, 368, 903
Reynolds, C. S., & Begelman, M. C. 1997, ApJ, 487, L135
Reynolds, C. S., Brenneman, L. W., & Garofalo, D. 2005, Ap&SS, 300, 71
Reynolds, C. S., & Nowak, M. A. 2003, Phys. Rep., 377, 389
Ross, R. R., & Fabian, A. C. 1993, MNRAS, 261, 74
Ross, R. R., & Fabian, A. C. 2005, MNRAS, 358, 211
Shih, D. C., Iwasawa, K., & Fabian, A. C. 2002, MNRAS, 333, 687
Takahashi, T., et al. 2007, PASJ, 59, S35
Tanaka, Y., et al. 1995, Nature, 375, 659
Taylor, R. D., Uttley, P., & McHardy, I. M. 2003, MNRAS, 342, L31
Turner, A. K., Fabian, A. C., Lee, J. C., & Vaughan, S. 2004, MNRAS, 353, 319
Turner, A. K., Fabian, A. C., Vaughan, S., & Lee, J. C. 2003, MNRAS, 346, 833
Vaughan, S., & Edelson, R. 2001, ApJ, 548, 694
Vaughan, S., & Fabian, A. C. 2004, MNRAS, 348, 1415
Wilms, J., Reynolds, C. S., Begelman, M. C., Reeves, J., Molendi, S., Staubert, R., & Kendziorra, E. 2001, MNRAS, 328, L27
Yaqoob, T., et al. 2007, PASJ, 59, S283
Young, A. J., Lee, J. C., Fabian, A. C., Reynolds, C. S., Gibson, R. R., & Canizares, C. R. 2005, ApJ, 631, 733